01 Jan 2023

Evaluating Blast Wave Overpressure From Non-spherical Charges Using Time Of Arrival From High-speed Video

Kelly Williams

Catherine E. Johnson
Missouri University of Science and Technology, johnsonce@mst.edu

Recommended Citation

K. Williams and C. E. Johnson, "Evaluating Blast Wave Overpressure From Non-spherical Charges Using Time Of Arrival From High-speed Video," *Propellants, Explosives, Pyrotechnics*, Wiley, Jan 2023.
The definitive version is available at https://doi.org/10.1002/prep.202200346

Received: 16 December 2022 | Revised: 20 March 2023 | Accepted: 22 March 2023

DOI: 10.1002/prep.202200346

Propellants, Explosives, Pyrotechnics

RESEARCH ARTICLE

Evaluating blast wave overpressure from non-spherical charges using time of arrival from high-speed video

Kelly Williams | **Catherine E. Johnson**

Department of Mining and Explosives Engineering, Missouri University of Science and Technology, Rolla, (USA)

Correspondence
Dr. Catherine E. Johnson, Department of Mining and Explosives Engineering, Missouri University of Science and Technology, Rolla, MO 65409 (USA).
Email: catherine.johnson@mst.edu

Funding information
Johnson Graduate Group

Abstract

Scaled distance is used to predict blast wave overpressure surrounding the detonation of a known mass of explosive under the assumption that the charge geometry is spherical. Altering charge geometry from spherical overdrives regions of the blast wave resulting in areas of higher overpressures than predicted by scaled distance calculations. Empirical data can be used to scale the blast wave overpressure to cylindrical charges, but available overpressure data for more complex geometries is not available in published literature. In the present study the time of arrival of the blast wave was measured from high-speed video and the Rankine-Hugoniot relationship used to measure blast wave overpressure for varied explosive geometries. The radial overpressure of prismatic charges with cross-sectional shapes of triangle, rectangle, and 5-point star isotropic were compared to the radially isotropic overpressure distribution produced by a cylindrical explosive charge. The rectangle produced the highest overpressure measuring 3.5 times that of the cylinder while the triangular charge had the greatest presented surface area and was only overdriven 3.0 times. From the high-speed video the fireball of detonation products surrounding the star appears significantly overdriven from the internal angle, but this orientation was underdriven at 2.0 meters. The blast wave overpressure downstream from the outside corners of the rectangular and triangular prismatic charges were similar to that of the cylinder at 1.5 meters but trended higher at increasing distance.

KEYWORDS
blast wave, geometry, high speed imaging, scaled distance

1 | INTRODUCTION

A shock wave is a compression wave in which the peak pressure exceeds the yield strength and the velocity exceeds the speed of sound in the medium of travel [1–14]. In a reactive medium such as the secondary explosive mixture consisting of 50/50 blend of 1,3,5-trinitroperhydro-1,3,5-triazine (RDX) and 2,4,6-trinitrotoluene (TNT) known as Cyclotol 50/50 [15], a shock wave can initiate the chemically driven detonation reaction and is referred to as a detonation wave [16]. The detonation wave will radiate from the initiation point until reaching the explosive air boundary where the explosively generated shock wave transitions from a detonation wave inside the explosive charge to a blast wave in the air. The transition from detonation wave to blast wave is referred to as breakout [16–17]. In an idealized center point initiated free floating sphere, breakout occurs at the same time across the entire surface of the sphere transmitting a spherical, primary, blast wave into

the surrounding air. In non-spherical charges, bridge waves are formed at the corners of the charge resulting from the reflection of primary waves from adjacent sides as shown in Figure 1 [17–18]. Preliminary work using modified plate dent tests showed that blast wave overdriving originated at the explosive air boundary during breakout when reaction zone jetting overdrives the primary waves [19].

The blast wave can be divided into three fields with increasing radius, originating at the initiation point. First, the fireball field extends from the initiation point into the surrounding air out to the radius at which the blast wave and the fireball of detonation products separate, referred to simply as separation [6]. The fireball field is challenging to instrument due to the extreme heat, pressure, and light released during detonation. The second cited field in literature is the near field, which begins at separation and extends until blast effects are minimized, and which point is referred to as the far field. The transition between near and far field used for this research is a scaled distance of 0.72 $m/g^{1/3}$ which is commonly referred to as K-18 and a used as a safe distance for personnel during breaching [20]. Scaled distance is traditionally calculated using Eq. (1) in which Z is scaled distance, R is the radius in meters, and M is the TNT equivalent weight of the explosive charge.

$$Z = \frac{R}{W^{1/3}} \tag{1}$$

In a study of cylinders with varying length to diameter (L/D) ratios Wisotski commented that the primary waves from the sides of the cylinder were significantly overdriven relative to a sphere of the same mass. The side of the cylinder that produced the highest peak overpressure changed from the flat ends to the curved side as L/D decreases, and Wisotski noted that the peak overpressure originated from the side with the greatest presented surface area [17]. Presented surface area was not defined any further by Wisotski and brings to question if the curved surface area of the cylinder behaves differently than the flat ends of the cylinder.

Stoner and Bleakney published a study of spheres, cylinders, and a prism with a square cross section in which they commented that the physical presence of the gauge and mount creates a shadow zone in the blast wave, which significantly alters the waveform and pressure readings downstream. They noted that using an offset of 9 degrees did not produce downstream interference in the time of arrival data. The square prism of TNT was only instrumented normal to one of the flat sides, where the primary wave was overdriven and it was predicted that the bridge wave regions were underdriven [21, 22].

McNesby presented an optical method that uses a high-speed camera to record v(t) data eliminating the need for complex transducer arrays and the errors associated with improper placement [23]. The optical method allows multiple overpressure measurements to be taken along a selected orientation from a single event without the blast wave interference caused by the transducers and mounts. Blast wave velocity is equated to blast wave overpressure using the Rankine Huguenot equation shown in Eq. (2) [23]. The variables in Eq. (2) are defined as P_x is the atmospheric pressure and P is the blast wave overpressure and M_x is the Mach number for the blast wave front.

$$P/P_x = (7M_x^2 - 1)/6 \tag{2}$$

The optical method does not directly generate a pressure versus time (p(t)) waveform, however within the near field the blast wave p(t) waveform is well described by the Friedlander equation shown in Eq. (3). The variables of the Friedlander equation are defined as: P_0 represents the ambient pressure, P_s is the pressure of the blast wave, t is time, and t^+ is the positive phase duration. Time of arrival (TOA) data can be used to populate the

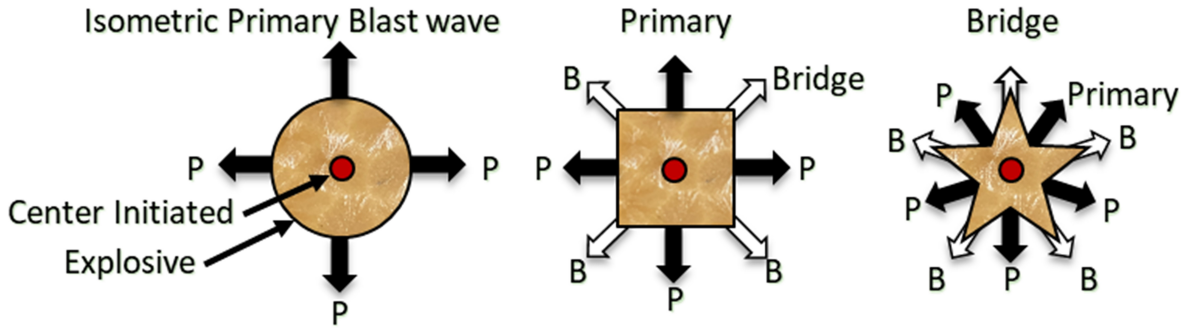

FIGURE 1 Blast wave after breakout from a circle, square, and star.

variables and plot a p(t) waveform that closely resembles a waveform recorded from a pressure transducer [24].

$$P_0 = P_s e^{-t/t^+}\left(1 - \frac{t}{t^+}\right) \quad (3)$$

The investigation detailed in this paper was designed to evaluate near field overpressure from non-spherical charges using an optical method in which the Rankine-Hugoniot equation is used to calculate overpressure in the near field from blast wave TOA taken from high-speed video of the event. Once the optical method was validated using pressure transducers, blast wave overpressure of primary and bridge waves produced by altering charge cross sectional shape was evaluated. A circle of the cylindrical charge was used as the control and compared to prismatic charges with varying cross-sectional shapes of a triangle, rectangle, and a 5-point star to determine anisotropic effects of explosive geometry on blast wave propagation.

2 | METHODOLOGY

In order to evaluate blast wave propagation for non-spherical charges from multiple angles without impeding the blast wave propagation due to sensors and stands, a method using high speed imaging to evaluate overpressure was used. This section outlines the methodology and validation of the optical pressure measurement system as well as the experimental test setup to compare blast propagation from prismatic charges with rectangle, triangle and five-point star cross sections.

2.1 | Methodology and validation of an optical toa pressure measurement system

High-speed imaging and the accompanying analysis software make it possible to measure the change in the shock front position between images by calibrating pixel size to a fiducial in the image. The velocity of the blast wave can then be calculated by dividing the change in position between the two frames by the time elapsed between the two frames. To determine whether accurate pressure measurements are possible using the available high-speed camera to determine time of arrival at two known points in time for use in Eq. (1), a validation experiment was designed and conducted with cylindrical charges. The test setup was instrumented with two dual transducer integrated electronic piezoelectric pressure sensors (PCB 137B25) sampled with a data acquisition system (Hi-Techniques Synergy P) at 2 MHz for comparison to pressure measurements from the optical method. Four cylindrical 285 ± 0.4 gram (g) charges with an average density of 1.59 grams per cubic centimeter (g/cm^3) were melt cast using Cyclotol 50/50 sourced from Bicoastal cast boosters [25–26]. The molds were made by plugging one end of a 0.25 meter (m) section of 0.038 m diameter schedule 40 PVC pipe with a 0.050 m long wooden plug. Extra pipe length was left beyond the charge length to assist with removing is once the charge cooled. The plug was center drilled to accept a cap well insert to create a 0.013 m deep cap well for a #8 electric detonator. To suspend the charge without interfering with the radial expansion of the shock wave a 0.5 m length of 23-gauge wire was cast through the charge along the central axis, labeled as "suspension wire" in Figure 2.

The testing was conducted on a concrete blast pad to facilitate repeatable layout of the pencil probe and charge stands which were anchored to the pad with a turnbuckle. The pencil probes were placed at 0 and 180 degrees in the radial plane surrounding a cylindrical charge to record overpressure versus time at a radius of 1.52 m which equates to a scaled distance of 0.21 $m/g^{1/3}$ as shown in Figure 3. The camera (Phantom v2012 [27]) was set to record the propagation of the shock wave in 180 degrees of the radial plane of the cylindrical charge with a field of view of 3.2 by 1.6 m, and a frame rate of 92,000 frames per second as shown in Figure 3. Overpressure was calculated at a radius of 1.52 m every 15 degrees from 0–180 degrees. The charge was suspended 1.52 m above the blast pad by attaching the wire cast along the central axis of the cylinder to two stands that were anchored to the concrete pad 3.0 m away from each other. Two similar stands held the dual transducer pencil probes, which were also set 1.52 m off the blast pad and 3.0 m apart. The blast wave will reach the concrete pad at the same time it reaches the front transducer in the pencil probes to eliminate the interference of the ground reflection on the waveform. The firm anchoring on a substantial level surface of the concrete blast pad provided a very repeatable test setup with little movement or adjustment required between iterations.

Each of the cylindrical charges was initiated with an electric blasting cap inserted into the cap well cast into the end of the charge facing the camera. A break wire setup consisting of an enamel-coated 35-gauge wire looped over the end of the electric cap and connected to the trigger input of the camera. The trigger output from the camera provides a 5 volt signal to the data acquisition system (DAS) that drops to 0 volts when the camera is triggered. For redundancy, the DAS was set to begin recording if the voltage signal from the camera trigger output signal drops below 5 volts, or when a pressure spike occurred from one of the pressure transducers.

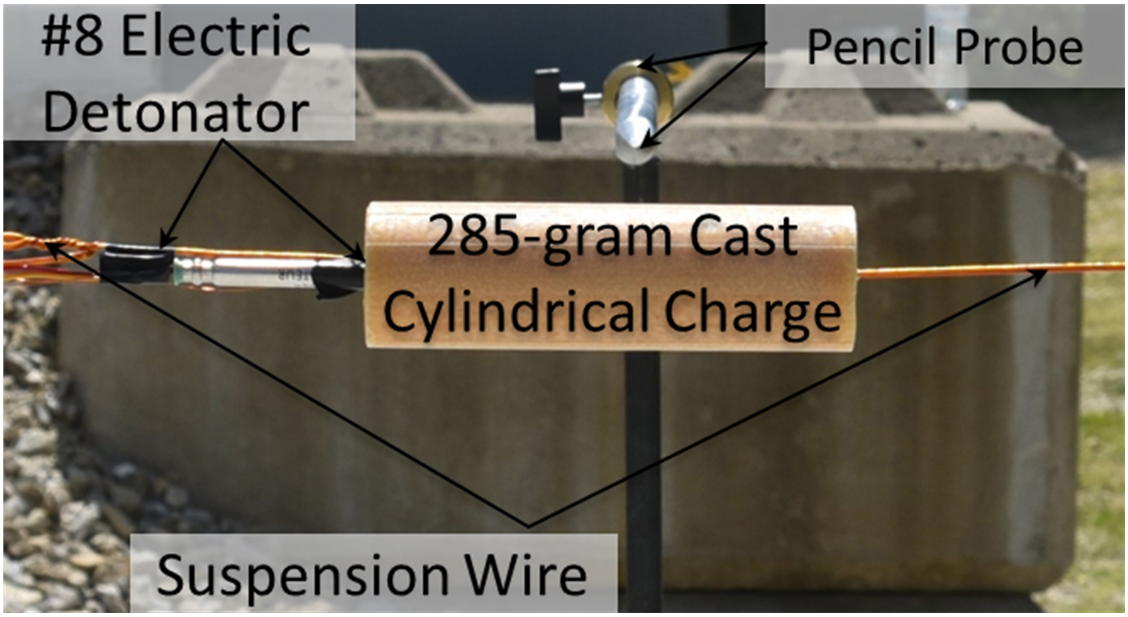

FIGURE 2 Close up of suspended charge and pencil probe taken from just above the 0° pencil probe.

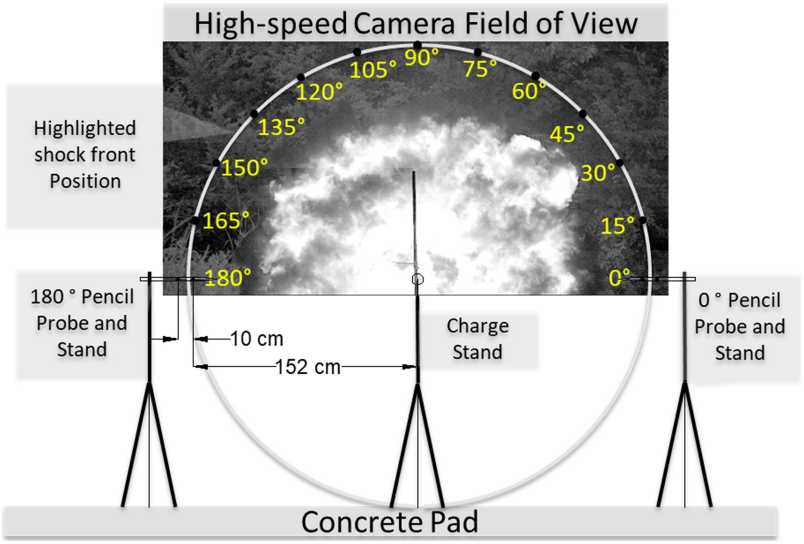

FIGURE 3 Annotated image from High-speed video illustrating the 3.2×1.6 m camera field of view and the position of the pressure transducers used as a fiducial to calibrate image measurement tools and validate pressure measurements made with the optical TOA method.

The optical overpressure at 1.52 m was calculated and compared to the overpressure recorded from the pressure transducers. The average optical overpressure from four detonations at the transducer radius of 1.52 m is 166.0 ± 3.8 kPa which is within the deviation range of the overpressure measured with the pressure transducers of 164.6 ± 7.6 kPa indicating that the high-speed imaging TOA method can be used to measure blast wave overpressure as accurately as pressure transducers for blast wave propagating into ambient air. Based on the tests and analysis conducted in the validation study, a number of improvements were identified to the casting and initiating process as well as the optimal field of view for near field pressure measurements. These changes were implemented in the geometry study and described in the following section.

Part of the reason for the higher deviation in the pressure transducer measurements could result from error in measuring the distance from the charge to the transducers. If the transducers are equidistant from an isometric shock wave, the time of arrival of the shock front should be equal. The time of arrival at the pressure

transducers were 1.215 and 1.223 ms at 0 and 180 degrees, respectively. At the average optically measured blast wave velocity of 545 m/s, the 0.008 ms difference indicates that the transducers radii were within 0.004 m assuming the blast wave radius was perfectly isometric. Even this slight deviation in transducer placement highlights the challenge of accurately setting the position of pressure transducers.

Cooper provides a chart for predicting blast wave overpressure from scaled distance using a modified version of the scaled distance equation shown in Eq. (4) in which Z_c is scaled distance, R is the radial distance to the blast wave front, W is the TNT mass equivalency of the charge, T_a is the ambient air temperature, and P_a is the ambient air pressure.

$$Z_c = \frac{R}{\left(WT_a/P_a\right)^{1/3}} \tag{4}$$

In Cooper's example the TNT equivalence is calculated using Eq. (5) by dividing the square of the velocity of detonation (VOD) of the charge by the VOD of TNT. Using the VOD of the 50/50 charge of 7.83 km/s [19] and the VOD of TNT of 6.95 km/s [16] yields a TNT equivalency of 1.27, and Z_c of 0.315 m/kg$^{1/3}$. Using a Z_c of 0.315 m/kg$^{1/3}$, and an ambient pressure of 1.018 bar, Cooper's figure 28.2 gives a predicted blast wave overpressure of 132.3 kPa.

$$\text{TNT equivalence} = \frac{\left(VOD_{Charge}\right)^2}{\left(VOD_{TNT}\right)^2} \tag{5}$$

Because the empirical data used to generate Cooper's figure 28.2 uses spherical charges it is necessary to convert it to a cylindrical charge. Using Swisdak's figure 11.a provides a conversion factor of 1.48 [24], resulting in a predicted blast wave overpressure of 196 kPa. The measured overpressure of 165 kPa was only 85% of the value predicted by Cooper's method, so the variables of charge density and initiation method were modified in an attempt to more closely match the predicted values.

Wisotski published a chart of radial overpressure versus length to diameter (L/D) ratios from cylindrical Composition B (Comp-B) charges at varying scaled distances [17]. The cylindrical charges used in the validation testing had an L/D ratio of 3.2 which would produce an overpressure of 190 kPa for the 285 g charges at a radius of 1.52 m. Although the work published by Wisotski used a 60/40 mix of RDX/TNT compared to the 50/50 in this work, there is still a strong correlation to the Cooper method calculation and need to improve the casting method used to increase the overpressure of the charges used in future studies.

The cylindrical charges used in the validation testing were cast in commercially available poly vinyl chloride (pvc) pipe, but the more complex prismatic charges would require custom fabrication. Brass was selected as the mold material because it is non-sparking, generally non-reactive, easily machinable, and can be warmed prior to pouring to slow the crystallization of the Cyclotol 50/50. With the goal of decreased internal voids and increased density the Cyclotol 50/50 charges for the next series of tests the molten Cyclotol 50/50 was poured into brass molds that were warmed to 60 degrees Celsius. The filled molds were stored in insulated containers to increase solidification time resulting in a consistent crystal structure within the charges. Void spaces occur in pour cast Cyclotol 50/50 charges when the outside of the charge solidifies first, and the internal composition continues to shrink as it cools and solidifies. Slowing the cooling process significantly reduces the temperature gradient between the inside and outside of the explosive charge and the shrinkage occurs at the top of the charge which is then topped off with a small amount of molten Cyclotol 50/50.

The cap well and electric detonator were replaced with a surface mounted exploding bridge wire (EBW) initiator held in place with ethylene vinal acetate adhesive. The EBW has an increased energy output over that of the electric detonator and is believed to drive the detonation wave up to full steady state faster and more consistently than the electric blasting caps used in the validation test series. The high voltage signal from the EBW initiation system was picked up by the DAS and assigned as trigger time for the data recording which provided a consistent t_0 for the p(t) waveforms.

2.2 | Evaluation of blast wave anisotropy from prismatic charges

An optical TOA method developed to measure blast wave overpressure was demonstrated to measure overpressure as accurately as modern pressure transducers. The optical TOA methodology was then used to evaluate pressure surrounding non uniform explosive charges. A series of tests was performed to measure overpressure surrounding 285 g charges with the same composition as the validation tests at 1.5 and 2.0 m. The charge size and distance equate to, 0.21 and 0.28 m/g$^{1/3}$, respectively which is within the near field. Prismatic charges with cross-sectional shapes of a rectangle, triangle, and 5-point star were evaluated and compared to that of a cylinder. For a single comparison pressure point, and fiducial marker, a pressure transducer, was placed at 1.5 m and 2.0 m for each test. To accommodate the increased

distance from the initiation point up to 2.0 m, the field of view for the high-speed camera was 2.2 × 2.2 m and filmed at a frame rate of 80,000 frames per second in order to maintain a similar propagation of error and increase measurement radius. One quadrant of the explosive detonation products and blast wave expansion were recorded for each shape, in contrast to the 180 degree window, or two quadrants, recorded in the validation tests. Two repetitions were conducted for each geometry, aside from the triangle where two repetitions were tested with the charge orientated with the point up, and two tested with the point down. The results of this investigation along with conclusions and references are detailed in the following sections.

3 | RESULTS AND DISCUSSION

Figure 4A–C shows images from the circle, triangle, and rectangular charges mirrored about the x and y as applicable to visualize the entire fireball. The triangle and rectangle both produce overdriven fireballs in in the primary orientations and underdriven bridge waves from the corner, illustrated by the fireball extending beyond or under the dashed line representing the radius of the cylindrical charge at the same time step after initiation.

The 360 degree image for the star shown in Figure 5 was made by rotating the image about the center point. The star produced significant overdriving from the primary waves from the interior angles of the star and significant underdriving from the bridge waves from the outside corners of the charge. It appears from these images that the most significant overdriving will occur from the primary waves from the shorter sides of the triangle and rectangle and from the primary waves of the star which contradicts Wisotski's observation that the highest overpressure comes from the side with the greatest presented surface area.

The optical TOA method consists of a series of radius versus time measurements taken from high-speed images at approximately 0.05 m increments. Two repetitions were measured at 0, 45, and 90 degrees surrounding the cylindrical charge. Velocity is calculated over 6 frames from the video to reduce the margin of error of the method. Velocity versus radius is plotted in Figure 6 for the cylinders which shows the best fit line equation and the R^2 value of 0.9. The actual position of the blast wave front is used which results in the data points being scattered rather than grouped in vertical lines. In order to assign the overpressure measurement to a specific radius, the best fit line equation is used to calculate velocity at the selected radii which is used to calculate overpressure using Eq. (1).

The optical pressure for the circle at 1.5 and 2.0 m calculated from the best fit line equation was input into the Friedlander equation to model the blast waveform at those radii. These waveforms in addition to the waveforms recorded from the pressure transducers at the same radii can be seen in Figure 7. At 1.5 m the optical overpressure measures slightly higher, and the decay of the transducer waveform is steeper than the Friedlander curve. The variation in the p(t) waveforms is considered negligible within the scope of this investigation but extending the overpressure calculations below 1.5 m is not advised without empirical validation. Extension of the best fit line to 2.0 m is shown to correlate well with pressure transducer data as shown by the practically equivalent waveforms for both pressure transducer and optically derived Friedlander curve at 2.0 m.

Figure 8 shows pressures for primary and bridge waves for all charges at a radius of 1.5 m, derived using the best fit line equation at that orientation and Eq. (1). At 1.5 m in the near field the overpressure surrounding

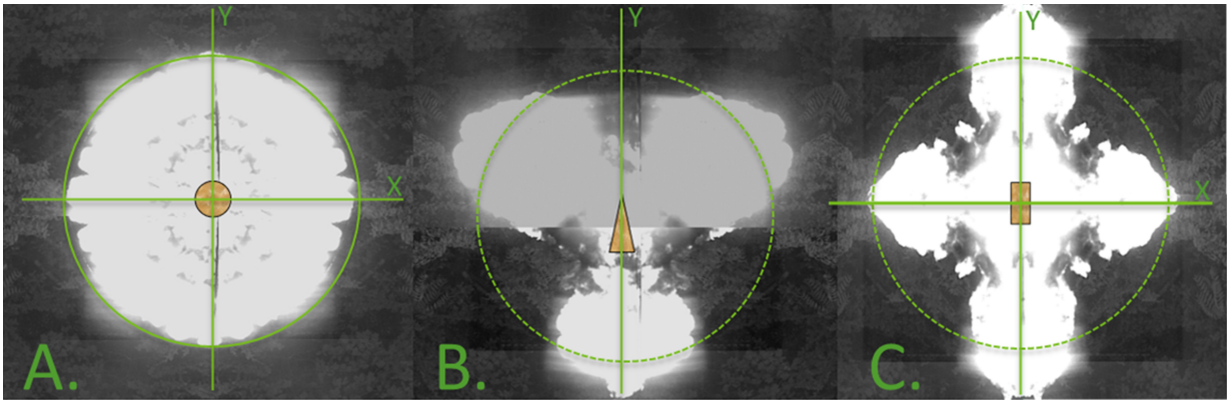

FIGURE 4 Images from the high-speed video at 0.5 ms, **A**. circle, **B**. triangle, and **C**. rectangle to illustrate relative fireball size at separation.

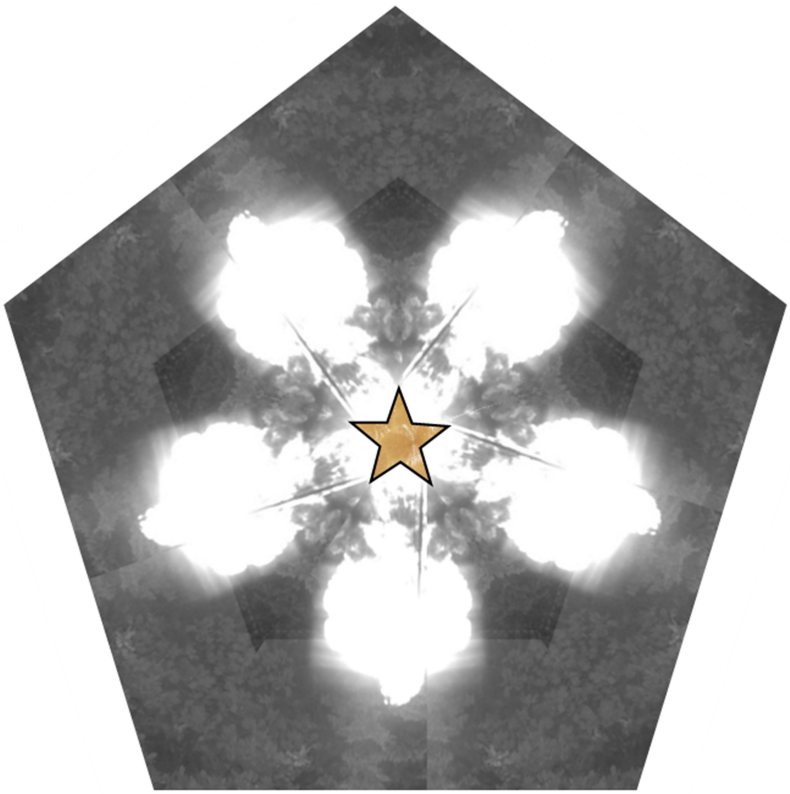

FIGURE 5 Fireball from the star prism at 0.5 ms after initiation.

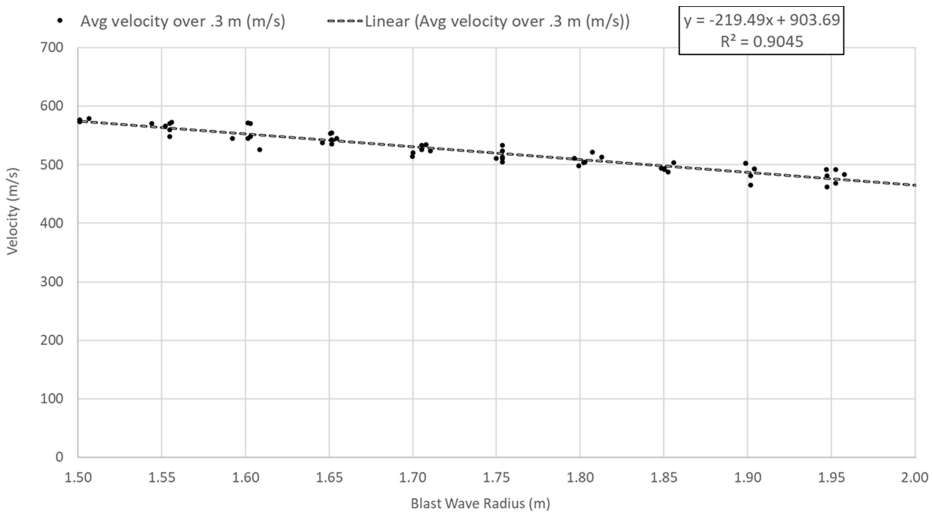

FIGURE 6 Chart of velocity versus radius for cylindrical charges.

the triangular prism is significantly higher normal to the sides than from the corners of the charge. Wisotski noted that the highest overpressure occurred downstream from the orientation with the highest presented surface area. Because length and cross-sectional area were kept constant for the charges used in this series of tests the length of the sides of the cross-sectional shapes would correlate directly with surface area. The longer side of the triangle was 0.069 m and produced a peak overpressure of 592.9 kPa. While the pressure is higher than the shorter side of the triangle, the primary wave from the 0.051 m side of the rectangle produced the highest overpressure at 1.5 m of 698.5 kPa indicating that while presented surface area does play a part in blast wave overpressure the number of sides, or the size of the angles at the corners of the charge may also influence blast wave shaping. This correlation is in contrast to the visual fireball extents in Figure 4 where the short

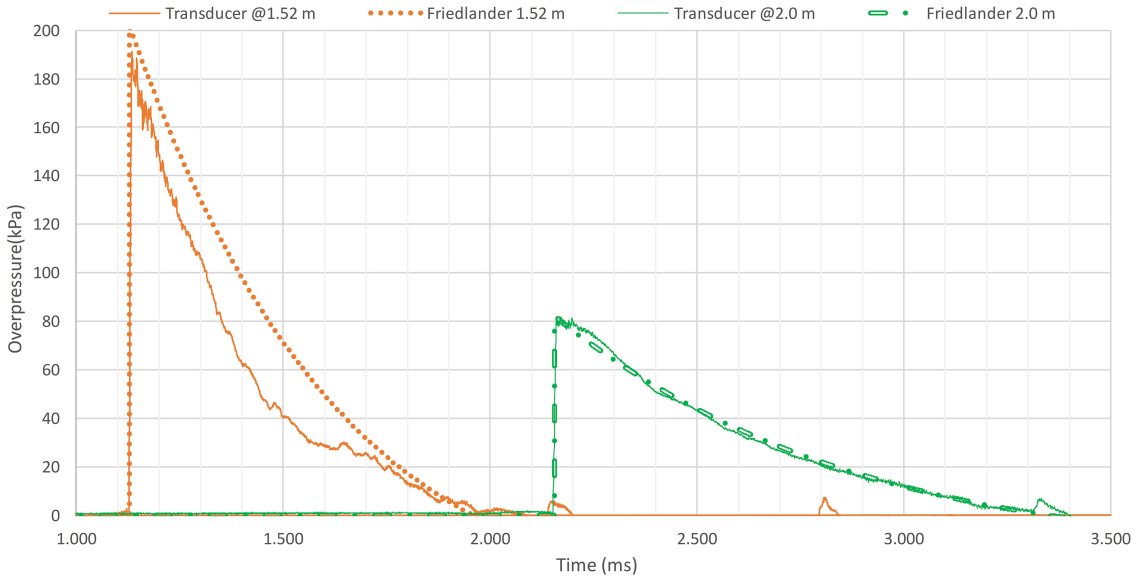

FIGURE 7 Pressure versus time waveforms recorded from transducers and Friedlander curve with peak pressure from optical TOA method.

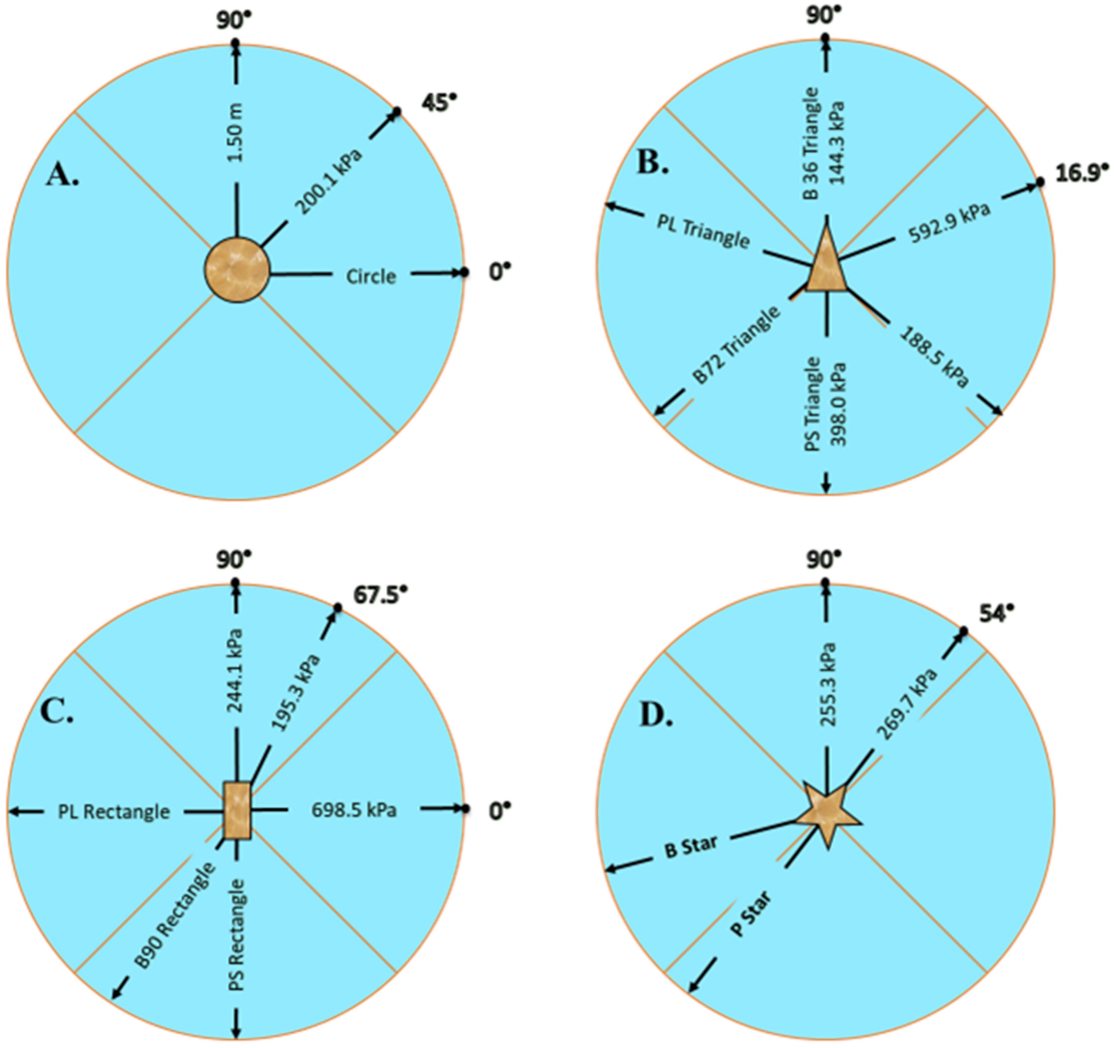

FIGURE 8 Primary (P) and Bridge (B) wave overpressures at 1.50 m surrounding **A**. circle, **B**. triangle, **C**. rectangle, and **D**. star.

sides of each shape extended the furthest. The average pressure for the circle cross section was 200.1 kPa, a 32 kPa increase over the same mass validation tests, and within 3% of the 196 kPa prediction from Cooper's method. There is no available data that provides a multiplier for prismatic charges, so the radial overpressure of the cylindrical charges is used as a baseline for comparison. This increase was due to the increase in density over the previous casting method in addition to the higher energy EBW initiator. Averaging the bridge wave pressures from all charges results in 199.5 kPa which is very similar to the average for the cylinder control of 200.1 kPa. The average pressure for primary waves of non-spherical charges was 437.8 kPa, which is 2.19 times that of the cylinder.

Figure 9 is a chart illustrating p(r) best fit lines for the primary wave peak overpressure from the rectangle, triangle, and circle. The best fit line for the circle falls from 200.1 kPa down to 90.0 kPa between 1.5 and 2.0 m. In the chart legends shown in Figure 9 the best fit lines are labeled Primary wave Long side (PL), Primary wave Short side (PS), followed by the cross-sectional shape of rectangle, triangle.

The primary waves from the rectangle and triangle are all overdriven in comparison to the circle at 1.5 m, but the rate of overpressure decay with increasing radius is higher for all the p(r) lines of the primary waves in relation to the circle. At 1.5 m the primary wave from the shorter side of the rectangle is overdriven by 1.2 times, and the two lines intersect at 1.7 m. The p(r) lines for the other primary waves rapidly approach the p(r) line of the circle and appear to crossover the p(r) line of the circle shortly beyond 2.0 m, after which the overpressure of the primary waves will be underdriven for the remainder of the near field.

The p(r) chart shown in Figure 10 shows the bridge waves from the triangle and rectangle in reference to the circle. In the legend, the lines are labeled as bridge wave (B) followed by the angle of the corner where the bridge wave originates and concluded with the cross-sectional shape of the charge of circle, rectangle, and triangle. Between 1.5 and 2.0 m the best fit lines for the bridge waves from the triangle and rectangle are similar to that of the circle. The bridge wave waveforms trend from slightly lower at 1.5 m to slightly higher at 2.0 m. Within the instrumented range, all three of the bridge wave p(r) lines cross over the circle and go from underdriven to overdriven. If the primary wave p(r) lines continue to diverge from the circle beyond 2.0 m the overpressure of the bridge waves could be significantly overdriven out to the far field.

The P(r) chart for the star and circle shown in Figure 11 show a trend similar to the primary waves in that both bridge and primary waves are higher at 1.5 m but decay faster with the line from primary wave of the star crossing over the circle at 1.75 m. It appears that for more complex geometries such as the star, the benefit of extreme overdriving of primary waves in the fireball field may come with the added benefit of decaying below damage thresholds at scaled safe distances near the extent of the near field.

The primary wave from the star produced significant overdriving of primary waves in the fireball field resulting in the significantly anisotropic radius of detonation

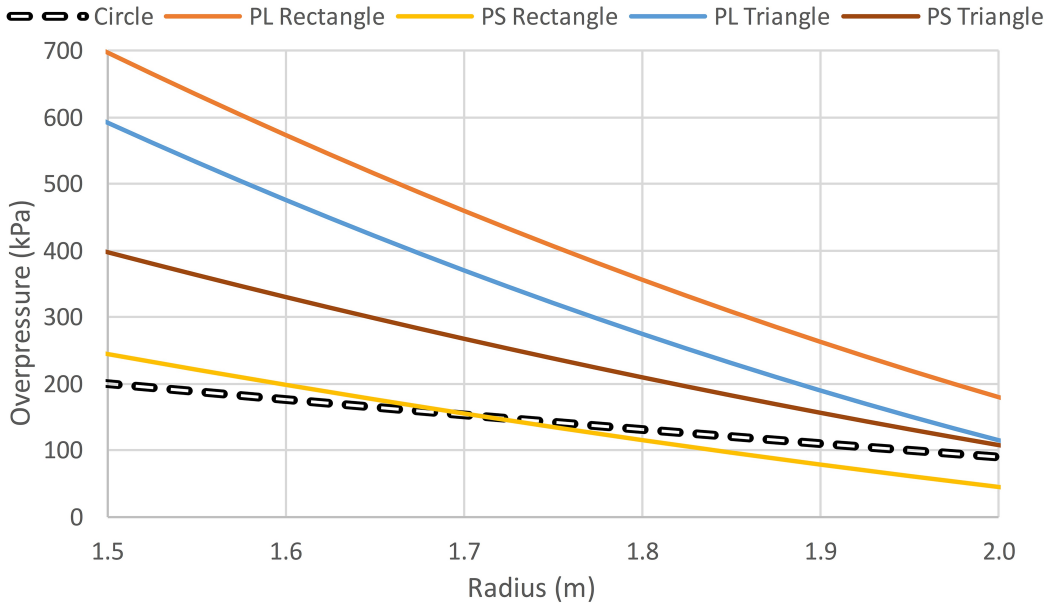

FIGURE 9 Pressure versus blast wave radius for cylindrical charges and primary waves from prisms.

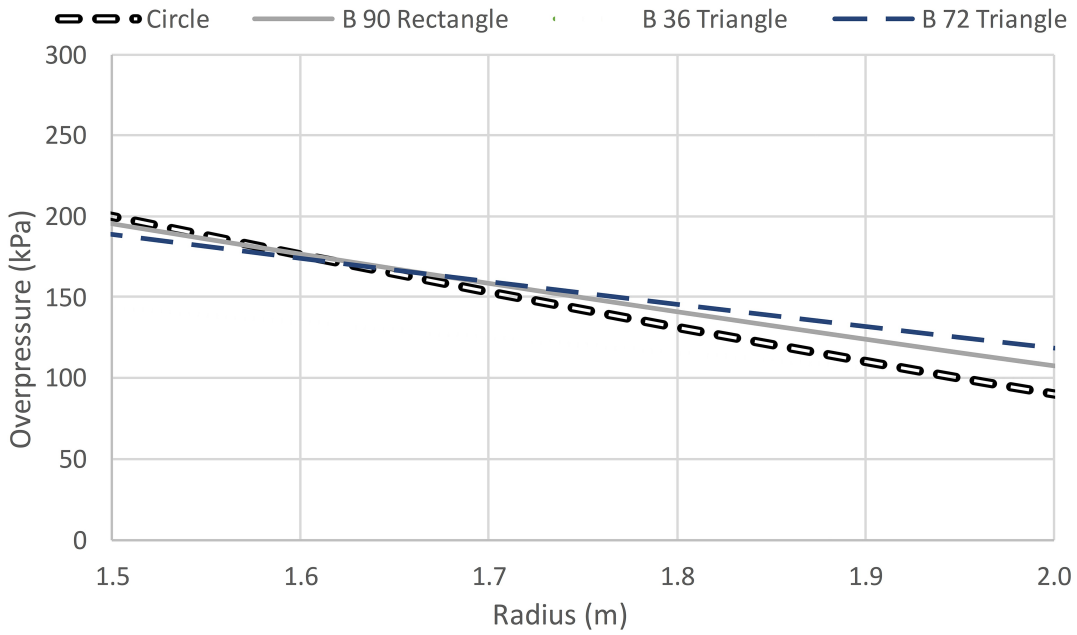

FIGURE 10 Pressure versus blast wave radius for circle and bridge waves from rectangle and triangle.

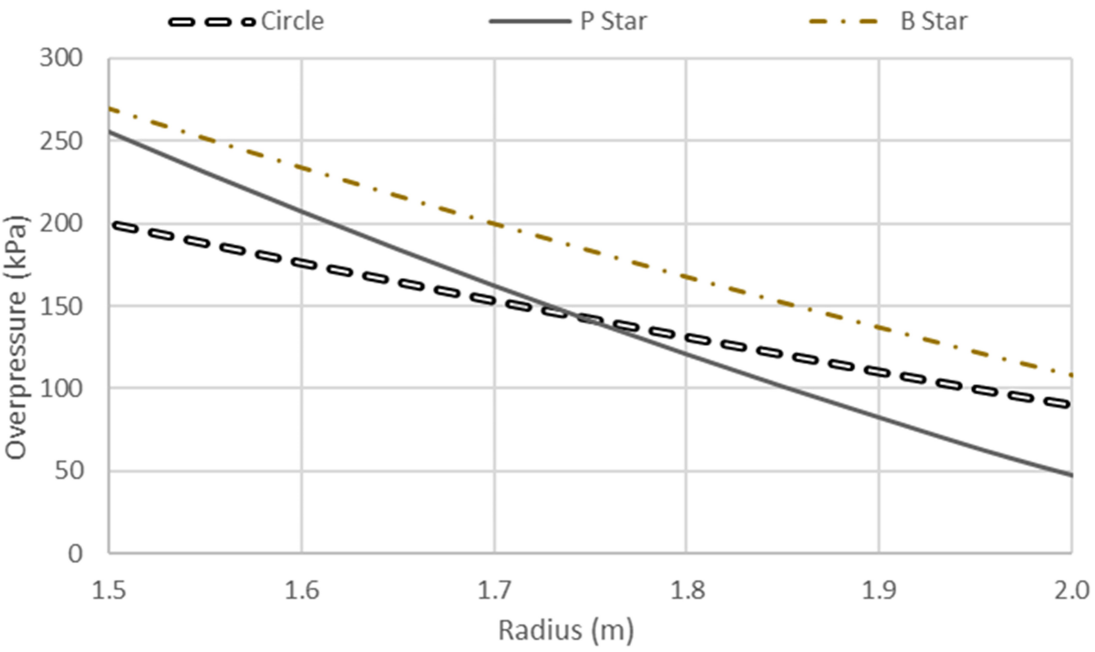

FIGURE 11 Pressure versus blast wave radius for circle and star at primary (P) and bridge (B) orientations.

products from the star shown in Figure 12. The fireball field radius extends significantly further from the interior angles of the star where the primary waves originate. The increased anisotropy in the radius and the extreme overdriving observed in the fireball field was theorized to result in higher primary blast wave overpressure in the near field, at the measured radii, primary and bridge waves from the star produced only a moderate initial pressure magnification that appears to decay below the overpressure of the circle with only a slight extension of the best fit lines beyond 2.0 m.

The bar graph in Figure 13 shows a summary of over and under driven characteristics from all tests using a pressure ratio calculated by dividing the pressure from the prism by that of the cylinders. A pressure ratio greater than 1 indicates overdriving and less than 1 underdriving. Primary waves are overdriven at 1.5 m and underdriven or trending towards the crossover point at

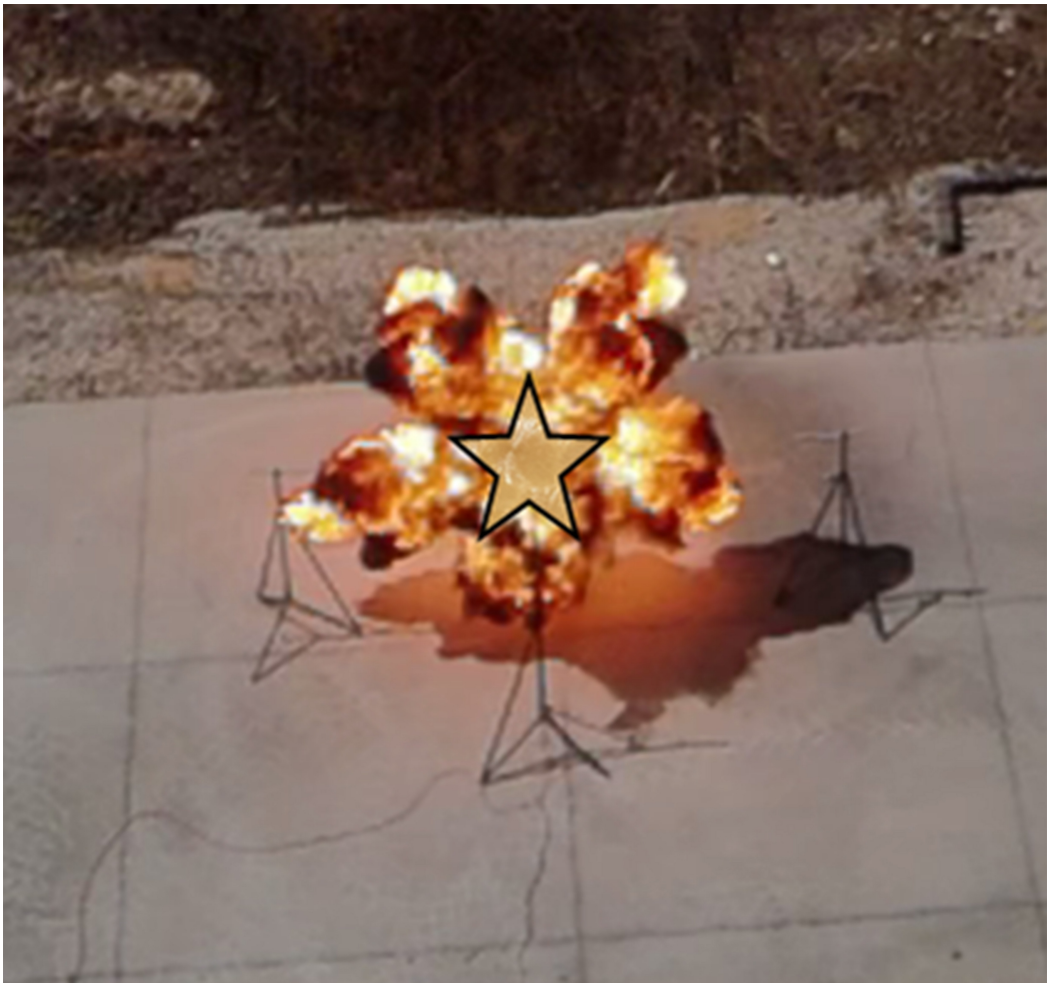

FIGURE 12 Fireball from the detonation of a star shaped prism annotated with star to show relative positions or fireball and charge.

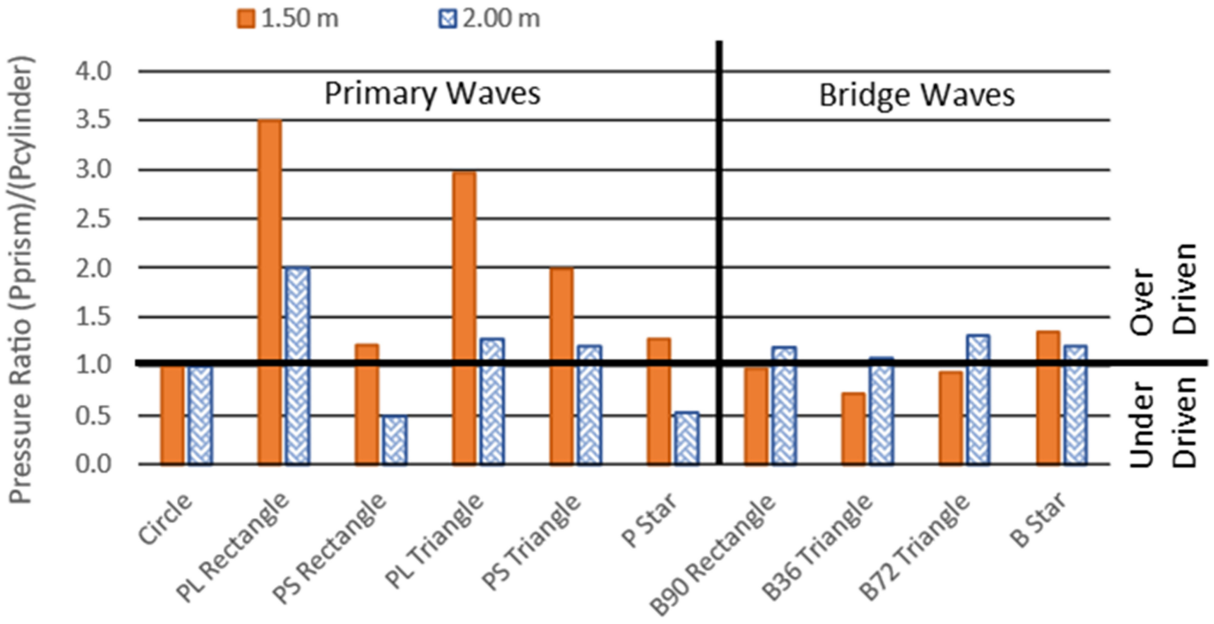

FIGURE 13 Bar graph of pressure ratios (Pprism/Pcylinder) for all shapes at 1.50 and 2.00 m.

2.0 m, indicating that the initially overdriven primary waves would be underdriven at the scaled distance safe radius. The bridge waves show an opposite trend of becoming more overdriven with increasing radius indicating that the bridge wave regions may be overdriven when they reach the scaled distance safe standoff radius of 4.7 m. For the star both the bridge and primary waves become more underdriven with increasing radius indicating that both primary and bridge waves from the star will be underdriven at the scaled distance safe standoff radius. The star demonstrated the highest degree of overdriving as measured at the explosive boundary with the modified plate dent test [20] but will be underdriven at scaled distance safe radius indicating that under some conditions blast wave overdriving can be used to significantly increase work output in the fireball field with the potential benefit of reduced overpressure at safe scaled distances.

4 | CONCLUSIONS

Using a validated optical TOA pressure measurement system, various prismatic charges were evaluated to determine the level of anisotropic blast wave effects. Maximum overpressure was shown to correlate with the presented surface area within the same charge. Longer sides of the triangles and rectangles produced higher overpressures than the shorter sides of the same shapes. The triangle had the greatest presented surface area of the charges with a pressure ratio of 3.0, but the rectangle produced the highest measured peak pressure at 698.5 kPa with a pressure ratio of 3.5. This deviation from Wisotski's observation indicates that while presented surface area is a strong predictor of blast wave overdriving in the near field, the angles at the corners of the sides also plays a significant role.

The primary waves of all prismatic charges appeared to enter the near field overdriven, but decay faster than the circle resulting in potential under driving at the near/far field boundary. The bridge waves all crossover from underdriven to overdriven within the 0.5 m instrumented range for this investigation. If these trends continue to the far field, scaled distance derived safe standoff distance would be satisfactory for primary waves, but the bridge waves may be overdriven at the near/far field boundary potentially resulting in overpressures beyond known damage thresholds. Further empirical testing is required before informing scaled distance safe distance calculations.

In the measured range of the near field, the star primary and bridge waves are both overdriven by 1.3 at 1.5 m. By the time the blast wave reaches 2.0 m the pressure ratios have fallen to 0.5 for the primary wave and 1.2 for the bridge wave from the star. If the best fit lines are extended beyond the data to 2.2 m both primary and bridge waves are underdriven. Empirical validation is required to extend the best fit lines beyond the data, but the optical TOA method has been demonstrated as a powerful tool for accurately measuring blast wave overpressure along a radial line and at multiple orientations. Now that the optical TOA method has been validated, it can be used to measure blast wave overpressure at scaled distances relevant to the minimum safe distance calculations to evaluate the potential overexposure to blast wave overpressure resulting from non-spherical charge geometry. The trend in the data indicates that charge geometry could be used to significantly increase work done within the fireball field and into the near field potentially without increasing overpressure at standoff radii deemed safe with current scaled distance calculations.

ACKNOWLEDGEMENT

Members of the Johnson Graduate Group assisted in the setup and testing of the experimental work and casting of explosives charges. Members include Martin Langenderfer, Emily Johnson, Rachel Bauer, Everett Baker, Cody Thomas, and Frank Schott. I would also like to thank the EMRGe center for making the brass molds for casting the charges.

CONFLICT OF INTEREST STATEMENT

The authors declare no competing financial interest.

DATA AVAILABILITY STATEMENT

Data is available within the article.

REFERENCES

1. Zhou, X. Q., & Hao, H. (2009). Mesoscale modelling and analysis of damage and fragmentation of concrete slab under contact detonation. *International Journal of Impact Engineering*, *36*(12), 1315–1326. https://doi.org/10.1016/j.ijimpeng.2009.02.010.
2. Whelan, D. J., & Bocksteiner, G. (1995). Velocity of detonation, charge diameter and critical diameter in unconfined RDX-driven heterogeneous explosives. *Journal of Energetic Materials*, *13*(1-2), 15–34. https://doi.org/10.1080/07370659508019342.
3. Ten, K. A., Evdokov, O. V., Zhogin, I. L., Zhulanov, V. V., Zubkov, P. I., Kulipanov, G. N., Luk'yanchikov, L. A., Merzhievskii, L. A., Pirogov, B. Y., Pruuél, É. R., Titov, V. M., Tolochko, B. P., & Sheromov, M. A. (2007). Density distribution at the detonation front of cylindrical charges of small diameter. *Combust Explos Shock Waves*, *43*(2), 204–211. https://doi.org/10.1007/s10573-007-0028-z.
4. Sochet, I., Gardebas, D., Calderara, S., Marchal, Y., & Longuet, B. (1995). Blast Wave Parameters for Spherical Explosives Detonation in Free Air. *OJSST*, *1*(2), 31–42. https://doi.org/10.4236/ojsst.2011.12004.

5. Chalivendra, V., Song, B., & Casem, D. (Eds.). (2013). *Dynamic Behavior of Materials, Volume 1: Proceedings of the 2012 Annual Conference on Experimental and Applied Mechanics.* Springer New York, 10.1007/978-1-4614-4238-7.
6. Needham, C. E. (2018). *Blast Waves.* Springer International Publishing, 10.1007/978-3-319-65382-2.
7. Cook, M. A. (1956). *Fundamental Principles of Wave Shaping*, in Proceedings Of Detonation Wave Shaping Conference, picatinny arsenal dover nj.
8. Settles, G. S. (2006). High-speed Imaging of Shock Waves, Explosions and Gunshots: New digital video technology, combined with some classic imaging techniques, reveals shock waves as never before. *American Scientist*, *94*(1), 22–31.
9. Mellor, C., James, H. R., & Goff, M. J. (2012). *A computational exploration of the differences between prompt and bow shock initiation of explosives by shaped charge jets.* Proceedings of the Conference of the American Physical Society Topical Group on Shock Compression of Condensed Matter 2011, Chicago, Illinois, pp. 287–290. 10.1063/1.3686275.
10. Krehl, P. (2009). *History of Shock Waves, Explosions and Impact.* Springer Berlin Heidelberg, 10.1007/978-3-540-30421-0.
11. Kinney, G. F., Graham, K. J., & Raspet, R. (1986). Explosive Shocks in Air, 2nd ed. *The Journal of the Acoustical Society of America*, *80*(2), 708–708. https://doi.org/10.1121/1.394030.
12. Giannuzzi, P. M., Hargather, M. J., & Doig, G. C. (2016). Explosive-driven shock wave and vortex ring interaction with a propane flame, Shock Waves, 26(6), pp. 851–857. 10.1007/s00193-016-0627-2.
13. Forbes, J. W. (2012). *Shock Wave Compression of Condensed Matter: A Primer.* Springer Berlin Heidelberg, 10.1007/978-3-642-32535-9.
14. Asimow, P. D. (2012). *Shock compression of preheated silicate liquids: Apparent universality of increasing Grüneisen parameter upon compression.* Proceedings of the Conference of the American Physical Society Topical Group on Shock Compression of Condensed Matter 2011, Chicago, Illinois, pp. 887–890. 10.1063/1.3686420.
15. Anderson, E. K., & Jackson, S. I., *Cyclotol Detonation Performance as a Function of Scale and Geometry*.
16. Cooper, P. W. (1996). *Explosives engineering.* VCH.
17. Wisotski, J., & Snyer, W. H. (1965). *Characteristics of blast waves obtained from cylindrical high explosive charges (U).* Naval Ordnance Laboratory (White Oak Md.), Denver Research Institute.
18. Baker, W. E. (1980). *Manual for the prediction of blast and fragment loadings on structures.* USDOE Albuquerque Operations Office, NM; Southwest Research Inst., San Antonio, TX (USA), DOE/TIC-11268, 10.2172/5892901.
19. Williams, K., & Johnson, C. E. (2021). Investigating anisotropic blast wave parameters near the explosive-air boundary using computer simulation and experimental techniques with varying charge geometry. *Journal of Applied Physics*, *130*(20), 205902. https://doi.org/10.1063/5.0068877.
20. Langenderfer, M., Williams, K., Douglas, A., Rutter, B., & Johnson, C. E. (2021). An evaluation of measured and predicted air blast parameters from partially confined blast waves. *Shock Waves*, *31*(2), 175–192. https://doi.org/10.1007/s00193-021-00993-0.
21. Stoner, R. G., & Bleakney, W. (1948). Erratum: The Attenuation of Spherical Shock Waves in Air. *Journal of Applied Physics*, *19*(12), 1129–1129. https://doi.org/10.1063/1.1715031.
22. Stoner, R. G., & Bleakney, W. (1948). The Attenuation of Spherical Shock Waves in Air. *Journal of Applied Physics*, *19*(7), 670–678. https://doi.org/10.1063/1.1698189.
23. McNesby, K. L., Biss, M. M., Benjamin, R. A., & Thompson, R. A. (2014). Optical Measurement of Peak Air Shock Pressures Following Explosions. *Propellants, Explosives, Pyrotechnics*, *39*(1), 59–64. https://doi.org/10.1002/prep.201300023.
24. M. M. Swisdak, Explosion Effects and Properties. Part I. Explosion Effects in Air, Naval Surface Weapons Center White Oak Lab, 1 975. Accessed: Nov. 29, 2021. [Online]. Available: https://apps.dtic.mil/sti/citations/ADA018544.
25. Customs Ruling NY N308367 – The tariff classification of an explosive mixture from China (2023, Feb. 23). https://www.customsmobile.com/rulings/docview?doc_id=NY%20N308367&highlight=3602.00.00%2A.
26. Bicoastal Boosters LLC (2022, Nov. 30). https://bicoastalusa.com/.
27. Phantom v2012 (2022, Sep. 04). https://www.phantomhighspeed.com/products/cameras/ultrahighspeed/%20v2012.

SUPPORTING INFORMATION

Additional supporting information can be found online in the Supporting Information section at the end of this article.

How to cite this article: Williams K. & Dr.Johnson C. E. (2023). Evaluating blast wave overpressure from non-spherical charges using time of arrival from high-speed video. *Propellants, Explosives, Pyrotechnics*, *48*, e202200346. https://doi.org/10.1002/prep.202200346

Graphical Abstract

The contents of this page will be used as part of the graphical abstract of html only. It will not be published as part of main.